

1 **Supporting Information for ”Multi-solver**  
2 **spectral-element and adjoint methods”**

Yujiang Xie<sup>1</sup>, Catherine Rychert<sup>1</sup>, Nicholas Harmon<sup>1</sup>

Qinya Liu<sup>2</sup>, Dirk Gajewski<sup>3</sup>

3 <sup>1</sup>Ocean and Earth Science, University of Southampton, UK

4 <sup>2</sup>Department of Physics & Department of Earth Sciences, University of Toronto, Canada

5 <sup>3</sup>Institute of Geophysics, University of Hamburg, Germany

6 Contents of this file

- 7 1. Fréchet kernels in three model parameter sets
- 8 2. Hessian kernels in three model parameter sets
- 9 3. Wavefield storage method (WSM) for computing Hessian kernels
- 10 4. Figures S1 to S17, where Figures S9 to S17 are shown for the WSM

**1. Fréchet kernels in three model parameter sets**

11 Fréchet kernels are related to the first-order derivatives of the seismic data functional,  $\chi$ .

12 Assuming the perturbation of the functional as  $\delta\chi$ , we may have (also see Tromp et al.,

---

13 2005)

$$14 \quad \delta\chi = \int_V \overline{K}_m \frac{\delta\mathbf{m}}{\mathbf{m}} d^3\mathbf{x} = \int_V K_m \delta\mathbf{m} d^3\mathbf{x}, \quad (1)$$

15 where  $\overline{K}_m$  or  $K_m$  denotes the *Fréchet* kernels, and  $V$  denotes the model volume. The  
 16 kernels applied to the perturbation of the model ( $\delta\mathbf{m}$ ) can be further expressed with  
 17 respect to three different model parameterizations as (see Tromp et al., 2005; Fichtner &  
 18 Trampert, 2011a)

$$19 \quad K_m \delta\mathbf{m} = \begin{pmatrix} K_\rho \\ K_\kappa \\ K_\mu \end{pmatrix}^T \begin{pmatrix} \delta\rho \\ \delta\kappa \\ \delta\mu \end{pmatrix} = \begin{pmatrix} K_\rho \\ K_\lambda \\ K_\mu \end{pmatrix}^T \begin{pmatrix} \delta\rho \\ \delta\lambda \\ \delta\mu \end{pmatrix} = \begin{pmatrix} K'_\rho \\ K_\alpha \\ K_\beta \end{pmatrix}^T \begin{pmatrix} \delta\rho \\ \delta\alpha \\ \delta\beta \end{pmatrix}, \quad (2)$$

20 where the superscript T denotes the vector transpose. The model parameters  $\rho$ ,  $\kappa$  and  $\mu$   
 21 indicate the density, bulk and shear moduli. The  $\lambda$  and  $\mu$  are the lamé parameters. The  $\mu$   
 22 used in the two sets of model parameters is the same. The  $\alpha$  and  $\beta$  are the compressional  
 23 and shear wave speeds. The *Fréchet* kernels can be further expressed by a cross-correlation  
 24 of the forward and adjoint fields as (see e.g., Tromp et al., 2005; Liu & Tromp, 2006)

$$25 \quad \begin{pmatrix} K_\rho \\ K_\kappa \\ K_\mu \end{pmatrix} = \begin{pmatrix} K_\rho(\mathbf{s}^\dagger, \ddot{\mathbf{s}}) \\ K_\kappa(\mathbf{s}^\dagger, \mathbf{s}) \\ K_\mu(\mathbf{s}^\dagger, \mathbf{s}) \end{pmatrix}, \quad \begin{pmatrix} K_\rho \\ K_\lambda \\ K_\mu \end{pmatrix} = \begin{pmatrix} K_\rho(\mathbf{s}^\dagger, \ddot{\mathbf{s}}) \\ K_\lambda(\mathbf{s}^\dagger, \mathbf{s}) \\ K_\mu(\mathbf{s}^\dagger, \mathbf{s}) \end{pmatrix}, \quad \begin{pmatrix} K'_\rho \\ K_\alpha \\ K_\beta \end{pmatrix} = \begin{pmatrix} K'_\rho(\mathbf{s}^\dagger, \ddot{\mathbf{s}}) \\ K_\alpha(\mathbf{s}^\dagger, \mathbf{s}) \\ K_\beta(\mathbf{s}^\dagger, \mathbf{s}) \end{pmatrix}. \quad (3)$$

26 Two approaches may be used in practice to compute the Fréchet kernels. One is the *field*  
 27 *storage method* which first saves the forward field in space and time from the forward  
 28 simulation, and then during the adjoint simulation, reads the corresponding time step  
 29 of the forward wavefield into the temporary memory to conduct the calculation for the  
 30 Fréchet kernel. During the time integration for kernels, only one step of the forward  
 31 wavefield is read in at one time, therefore there is no need to carry the entire forward  
 32 field in memory. The field storage method is suitable for small or local scale simulations,  
 33 but becomes computationally prohibitive for large or global scale simulations due to the  
 34 large amount of disk storage required and the frequent I/O calls. The second method

is the *forward-field back-reconstruction method* which trades CPU hours with storage requirements as it only saves a very small subsets of time steps of the forward field from the forward simulation, and during the adjoint simulation, reconstructs the forward field back in time to combine the forward and adjoint wavefield directly in memory for the kernel calculation. For a purely elastic kernel calculation, only the last state of the forward field needs to be saved as the start point for the backward reconstruction during the adjoint simulation (see Tromp et al., 2005; Liu & Tromp, 2006; Tromp et al., 2008). For the anelastic case, the parsimonious storage method (Komatitsch et al., 2016) can be used with one additional forward simulation to account for the attenuation for the adjoint source, and the forward fields are stored at selected checkpoints and recomputed during the adjoint simulation.

## 2. Hessian kernels in three model parameter sets

We use the Hessian operator as defined by Fichtner and Trampert (2011a), which may be rewritten as

$$H(\delta\mathbf{m}_1, \delta\mathbf{m}_2) = \int_V K_m^1 \delta\mathbf{m}_2 d^3\mathbf{x} = \int_V (H_a + H_b + H_c) \delta\mathbf{m}_2 d^3\mathbf{x}, \quad (4)$$

where  $K_m^1 = H_a + H_b + H_c$  denotes the Hessian kernels, which can be expressed differently with respect to different model parameterizations.

1. When the model is given by  $\rho$ ,  $\kappa$ , and  $\mu$ , we may have

$$H_a(\rho, \kappa, \mu) = \begin{pmatrix} K_\rho(\mathbf{s}^\dagger, \delta\ddot{\mathbf{s}}) \\ K_\kappa(\mathbf{s}^\dagger, \delta\mathbf{s}) \\ K_\mu(\mathbf{s}^\dagger, \delta\mathbf{s}) \end{pmatrix}, H_b(\rho, \kappa, \mu) = \begin{pmatrix} K_\rho(\delta\mathbf{s}^\dagger, \ddot{\mathbf{s}}) \\ K_\kappa(\delta\mathbf{s}^\dagger, \mathbf{s}) \\ K_\mu(\delta\mathbf{s}^\dagger, \mathbf{s}) \end{pmatrix}, H_c(\rho, \kappa, \mu) = \begin{pmatrix} 0 \\ 0 \\ 0 \end{pmatrix}. \quad (5)$$

2. When the model is given by  $\rho$ ,  $\lambda$ ,  $\mu$ , we may have

$$H_a(\rho, \lambda, \mu) = \begin{pmatrix} K_\rho(\mathbf{s}^\dagger, \delta\ddot{\mathbf{s}}) \\ K_\lambda(\mathbf{s}^\dagger, \delta\mathbf{s}) \\ K_\mu(\mathbf{s}^\dagger, \delta\mathbf{s}) \end{pmatrix}, H_b(\rho, \lambda, \mu) = \begin{pmatrix} K_\rho(\delta\mathbf{s}^\dagger, \ddot{\mathbf{s}}) \\ K_\lambda(\delta\mathbf{s}^\dagger, \mathbf{s}) \\ K_\mu(\delta\mathbf{s}^\dagger, \mathbf{s}) \end{pmatrix}, H_c(\rho, \lambda, \mu) = \begin{pmatrix} 0 \\ 0 \\ 0 \end{pmatrix}. \quad (6)$$

3. When the model given by  $\rho, \alpha, \beta$ , we may have

$$H_a(\rho, \alpha, \beta) = \begin{pmatrix} K'_\rho(\mathbf{s}^\dagger, \delta\ddot{\mathbf{s}}) \\ K_\alpha(\mathbf{s}^\dagger, \delta\mathbf{s}) \\ K_\beta(\mathbf{s}^\dagger, \delta\mathbf{s}) \end{pmatrix}, H_b(\rho, \alpha, \beta) = \begin{pmatrix} K'_\rho(\delta\mathbf{s}^\dagger, \ddot{\mathbf{s}}) \\ K_\alpha(\delta\mathbf{s}^\dagger, \mathbf{s}) \\ K_\beta(\delta\mathbf{s}^\dagger, \mathbf{s}) \end{pmatrix}, \quad (7)$$

$$H_c(\rho, \alpha, \beta) = \begin{pmatrix} \rho^{-1}K_\alpha(\mathbf{s}^\dagger, \mathbf{s})\delta\alpha + \rho^{-1}K_\beta(\mathbf{s}^\dagger, \mathbf{s})\delta\beta \\ \rho^{-1}K_\alpha(\mathbf{s}^\dagger, \mathbf{s})\delta\rho + \alpha^{-1}K_\alpha(\mathbf{s}^\dagger, \mathbf{s})\delta\alpha \\ \rho^{-1}K_\beta(\mathbf{s}^\dagger, \mathbf{s})\delta\rho + \beta^{-1}K_\beta(\mathbf{s}^\dagger, \mathbf{s})\delta\beta \end{pmatrix}. \quad (8)$$

Eq.(5)-eq.(8) show the link between *Fréchet* kernels (Tromp et al., 2005) and the Hessian kernels (Fichtner & Trampert, 2011a) for different model parameterizations. The  $H_b$  practically includes two parts: one is the  $H_b^{(m)}$  which is due to the perturbation of the model, and the other is the  $H_b^{(s)}$  which is due to the perturbation of the adjoint source. The  $H_b^{(m)}$  can be given in different model parameterizations as

$$H_b^{(m)}(\rho, \kappa, \mu) = \begin{pmatrix} K_\rho(\delta\mathbf{s}_m^\dagger, \ddot{\mathbf{s}}) \\ K_\kappa(\delta\mathbf{s}_m^\dagger, \mathbf{s}) \\ K_\mu(\delta\mathbf{s}_m^\dagger, \mathbf{s}) \end{pmatrix}, \quad (9)$$

$$H_b^{(m)}(\rho, \lambda, \mu) = \begin{pmatrix} K_\rho(\delta\mathbf{s}_m^\dagger, \ddot{\mathbf{s}}) \\ K_\lambda(\delta\mathbf{s}_m^\dagger, \mathbf{s}) \\ K_\beta(\delta\mathbf{s}_m^\dagger, \mathbf{s}) \end{pmatrix}, \quad (10)$$

$$H_b^{(m)}(\rho, \alpha, \beta) = \begin{pmatrix} K'_\rho(\delta\mathbf{s}_m^\dagger, \ddot{\mathbf{s}}) \\ K_\alpha(\delta\mathbf{s}_m^\dagger, \mathbf{s}) \\ K_\beta(\delta\mathbf{s}_m^\dagger, \mathbf{s}) \end{pmatrix}, \quad (11)$$

where  $\delta\mathbf{s}_m^\dagger$  indicates the approximate perturbed adjoint field due to only perturbation in the model. The  $H_b^{(s)}$  referred to the approximate Hessian kernels defined by Fichtner and Trampert (2011a), which could be also rewritten in three model parameterizations as

$$H_b^{(s)}(\rho, \kappa, \mu) = \begin{pmatrix} K_\rho(\delta\mathbf{s}_s^\dagger, \ddot{\mathbf{s}}) \\ K_\kappa(\delta\mathbf{s}_s^\dagger, \mathbf{s}) \\ K_\mu(\delta\mathbf{s}_s^\dagger, \mathbf{s}) \end{pmatrix}, \quad (12)$$

$$H_b^{(s)}(\rho, \lambda, \mu) = \begin{pmatrix} K_\rho(\delta\mathbf{s}_s^\dagger, \ddot{\mathbf{s}}) \\ K_\lambda(\delta\mathbf{s}_s^\dagger, \mathbf{s}) \\ K_\beta(\delta\mathbf{s}_s^\dagger, \mathbf{s}) \end{pmatrix}, \quad (13)$$

$$H_b^{(s)}(\rho, \alpha, \beta) = \begin{pmatrix} K'_\rho(\delta\mathbf{s}_s^\dagger, \ddot{\mathbf{s}}) \\ K_\alpha(\delta\mathbf{s}_s^\dagger, \mathbf{s}) \\ K_\beta(\delta\mathbf{s}_s^\dagger, \mathbf{s}) \end{pmatrix}, \quad (14)$$

77 where  $\delta \mathbf{s}_s^\dagger$  indicates the approximate perturbed adjoint field due to only perturbation in  
 78 the adjoint source.

## 2.1. Implementation

79 In principle, the approximate or full Hessian kernels can be computed by using ex-  
 80 isting spectral-element packages for wavefield generation with the perturbed wavefields  
 81 computed in advance. The challenge is to compute and use these fields on the fly  
 82 as shown in this work. Once these fields are computed for each or incremental time  
 83 step, the Hessian kernels can be calculated by using, e.g., the *compute\_kernels()* sub-  
 84 routine in the SPECFEM2D/3D packages ([https://geodynamics.org/cig/software/](https://geodynamics.org/cig/software/specfem2d/)  
 85 [specfem2d/](https://geodynamics.org/cig/software/specfem2d/) and <https://geodynamics.org/cig/software/specfem3d/>), where one  
 86 just needs to substitute the regular fields with the perturbed field as indicated in eq.(5)-  
 87 (14). Similar to Fréchet kernel calculation for each time step, the computation of Hessian  
 88 kernels is performed at individual time step. Since only one single time step of all fields and  
 89 the integrated kernels are kept in memory on the fly, the use of a sub-sampled calculation  
 90 may be unnecessary.

## 3. Wavefield storage method (WSM) for computing Hessian kernels

91 The Hessian kernels can be computed when the required fields are determined. To compute  
 92 the required fields, we design and use one forward simulation and three adjoint simulations  
 93 (see Figure S10). The forward simulation is to compute and save four forward fields,  
 94 that is  $\mathbf{s}(\mathbf{m}_1)$ ,  $\mathbf{s}(\mathbf{m}_2)$ ,  $\ddot{\mathbf{s}}(\mathbf{m}_1)$ ,  $\ddot{\mathbf{s}}(\mathbf{m}_2)$ , where  $\mathbf{m}_2 = \mathbf{m}_1 + v\delta\mathbf{m}$ . The first and second  
 95 adjoint simulations (Adjoint simulation I) are designed to compute and save the adjoint  
 96 fields  $\mathbf{s}_s^\dagger(\mathbf{m}_1)$  and  $\mathbf{s}_m^\dagger(\mathbf{m}_2)$ . The third adjoint simulation, the last one, is a simultaneous

97 adjoint simulation and the Hessian calculation (Adjoint simulation II), where the adjoint  
98 simulation is to compute the adjoint field  $\mathbf{s}^\dagger(\mathbf{m}_1)$  on the fly during the construction of  
99 Hessian kernels.

### 3.1. Models

100 We use two synthetic models and take the Specfem2D package as examples. The first  
101 model is a homogeneous model ( $\mathbf{m}_1$ ) and the second model is a perturbation model ( $\mathbf{m}_2 =$   
102  $\mathbf{m}_1 + \nu\delta\mathbf{m}$ ) relative to the homogeneous one (see Fig S9 for the compressional wave speed  
103 and the source and receiver geometry). We placed the scatter on the kernel path and set  
104 the scatter size close to the dominant wavelength to account for the perturbed fields. Both  
105 models are set to  $800\text{ km} \times 360\text{ km}$  in the horizontal and vertical direction. For the mesher,  
106 we use the internal mesher of the Specfem2D package. We placed 400 elements in the  
107 horizontal direction and 360 elements in the vertical direction, leading to  $\sim 500\text{ m}$  and  $\sim$   
108  $250\text{ m}$  grid-point spacing respectively for the mesher since  $5 \times 5$  Gauss–Lobatto–Legendre  
109 (GLL) points for each element are used. We use a dense element mesh for the model to  
110 eliminate the effects of grid-point intervals to the kernel imaging since we focus on the  
111 computation of Hessian kernels here. A detailed resolution analysis or the use of external  
112 mesher tools, one can refer to Fichtner and Trampert (2011b) and Peter et al. (2011).

113 The model material properties for the homogeneous model is set to density  $2900\text{ kg/m}^3$ ,  
114 compressional wave speed  $\alpha = 8000\text{ m/s}$  and shear wave speed  $\beta = 4800\text{ m/s}$ . We  
115 use +10% relative model perturbation to model  $\mathbf{m}_1$  and the scatter perturbation is of  
116  $10\text{ km} \times 10\text{ km}$  located within the path that links the source and the receiver (see Fig S9b).  
117 For simplicity and to show how the Hessian kernels are computed, we use a point source

and place it at  $(x, z) = (100 \text{ km}, -260 \text{ km})$ . A standard Ricker wavelet with the dominant frequency of 0.5 Hz is applied. So the minimum wavelengths for the P and S waves are 16 km and 9.6 km respectively. The receiver is placed at the model surface at  $(x, z) = (600 \text{ km}, 0 \text{ km})$ . For this example, we use 10,000 time steps with  $dt = 0.01 \text{ s}$  for the simulation. The number of time steps and the  $dt$  can be estimated by the model setup and the phases to be investigated.

### 3.2. Forward simulation

Typically, the forward simulation includes two simulations, one for the model  $\mathbf{m}_1$  and the other for model  $\mathbf{m}_2$ . Both can be performed individually or simultaneously. In the forward simulation, the fields computed at each time step or a incremental time step are saved for the two models. The seismograms for the two models are saved to compute the two adjoint sources  $\mathbf{f}^\dagger(\mathbf{m}_1)$  and  $\mathbf{f}^\dagger(\mathbf{m}_2)$ . To facilitate the simulation, we run the two simulations for the two models simultaneously since there are sufficient memory left for each CPU. The use of a simultaneous simulation for the two models is convenient since there one just needs to input the two models and the forward fields and seismograms are computed once a time. In the simultaneous simulation, there are  $\sim 160/100$  memory and  $\sim 180/100$  computational time required when compared to the use of the single simulation twice. The reduction in memory and computational time less than double is due to the same mesh database used for the simulation, excluding the two models imported externally. Figure S11 shows four time steps of the forward displacement fields and their perturbed fields computed from the two models. The perturbed forward fields are observed (see Figure S11i,f,c) when the forward fields pass through the scatter.

### 3.3. Adjoint simulation I

139 There are two adjoint simulations in the *Adjoint simulation I* stage (see Figure S10). The  
 140 first adjoint simulation is to compute and save the adjoint field  $\mathbf{s}_s^\dagger(\mathbf{m}_1)$ , which accounts for  
 141 the perturbation due to the adjoint source. The adjoint source  $\mathbf{f}^\dagger(\mathbf{m}_2)$  computed from the  
 142 measurements for model  $\mathbf{m}_2$  is used (see Figure S12 for a quick view), where we use the  
 143 traveltimes adjoint source (Tromp et al., 2005). Figure S13 shows four time steps of the  
 144 adjoint fields  $\mathbf{s}^\dagger(\mathbf{m}_1)$  and  $\mathbf{s}_s^\dagger(\mathbf{m}_1)$  and their perturbations  $\delta\mathbf{s}_s^\dagger$ . The time-reversed perturbed  
 145 adjoint fields  $\delta\mathbf{s}_s^\dagger$  (the third column in Figure S13) are weaker than the regular adjoint  
 146 fields (the first and the second column). The second adjoint simulation in the *Adjoint*  
 147 *simulation I* is to compute  $\mathbf{s}_m^\dagger(\mathbf{m}_2)$ , which accounts for the perturbation of the model,  
 148 where the adjoint source  $\mathbf{f}^\dagger(\mathbf{m}_1)$  (see Figure S12) computed from the measurements for  
 149 model  $\mathbf{m}_1$  is used. Figure S14 shows four time steps of the adjoint fields  $\mathbf{s}^\dagger(\mathbf{m}_1)$  and  
 150  $\mathbf{s}_m^\dagger(\mathbf{m}_2)$  and the perturbed fields  $\delta\mathbf{s}_m^\dagger$ . The time-reversed perturbed adjoint fields are  
 151 generated when the regular fields pass through the scatter (see Figure S14i,l).

### 3.4. Adjoint adjoint II

152 The *Adjoint simulation II* is a simultaneous adjoint simulation and the Hessian kernel  
 153 calculation, where the adjoint simulation is to compute  $\mathbf{s}^\dagger(\mathbf{m}_1)$  on the fly, which is triggered  
 154 by the adjoint source  $\mathbf{f}^\dagger(\mathbf{m}_1)$ . In the adjoint simulation, each time step or a skipped time  
 155 step of *the four forward fields and the two adjoint fields* (the saved fields) are read into  
 156 the temporary memory for constructing the Hessian kernels for that time step. The  
 157 final Hessian kernels are accumulated(integrated) by previous Hessian kernels computed  
 158 at each counted step. In the implementation, only one time step of the Hessian kernels

159 (i.e., the integrated Hessian kernels) is kept in the temporary memory until it is output  
 160 finally. Figure S15 shows four components of the Hessian kernels:  $H_a$ ,  $H_b^{(m)}$ ,  $H_b^{(s)}$ , and  
 161  $H_c$  computed in this simulation. The four components individually with respect to the  
 162 density can be computed when used  $\ddot{\mathbf{a}}(\mathbf{m}_1)$  and  $\ddot{\mathbf{a}}(\mathbf{m}_2)$ . Only two forward and two adjoint  
 163 fields need to be stored if without considering the density kernels.

164 Figure S16 shows the conventional Fréchet kernels, where only the  $K_\alpha$  component is  
 165 observed well since only the P phase on the seismograms is used for the adjoint source  
 166 calculation. Figure S17 shows the full Hessian kernels investigated for the same P phase.  
 167 The full Hessian kernels are obtained by summing the  $H_a$ ,  $H_b^{(m)}$ ,  $H_b^{(s)}$ , and  $H_c$  components  
 168 together, which includes the approximate Hessian kernels  $H_b^{(s)}$  (see second row in Fig-  
 169 ure S15). The computation of full Hessian kernels includes the computation of Fréchet  
 170 kernels as required by the  $H_c$  calculation. The disk space required for the WSM approach  
 171 is big even for the 2D example, it takes about 400 GB disk space to store the required fields  
 172 even if without considering the density perturbation for the density kernel calculation.

## References

- 173 Fichtner, A., & Trampert, J. (2011a). Hessian kernels of seismic data functionals based  
174 upon adjoint techniques. *Geophys. J. Int.*, *185*, 775–798.
- 175 Fichtner, A., & Trampert, J. (2011b). Resolution analysis in full waveform inversion.  
176 *Geophys. J. Int.*, *187*, 1604–1624.
- 177 Komatitsch, D., Xie, Z., Bozdağ, E., Andrade, E. S. d., Peter, D., Liu, Q., & Tromp, J.  
178 (2016). Anelastic sensitivity kernels with parsimonious storage for adjoint tomogra-  
179 phy and full waveform inversion. *Geophys. J. Int.*, *206*, 1467–1478.
- 180 Liu, Q., & Tromp, J. (2006). Finite-frequency kernels based on adjoint methods. *Bulletin*  
181 *of the Seismological Society of America*, *96*, 2383–2397.
- 182 Peter, D., Komatitsch, D., Luo, Y., Martin, R., Goff, N. L., Casarotti, E., ... Tromp,  
183 J. (2011). Forward and adjoint simulations of seismic wave propagation on fully  
184 unstructured hexahedral meshes. *Geophys. J. Int.*, *186*, 721–739.
- 185 Tromp, J., Komatitsch, D., & Liu, Q. (2008). Spectral-element and adjoint methods in  
186 seismology. *Communications in Computational Physics*, *3*, 1–32.
- 187 Tromp, J., Tape, C., & Liu, Q. (2005). Seismic tomography, adjoint methods, time  
188 reversal and banana-doughnut kernels. *Geophys. J. Int.*, *160*, 195–216.

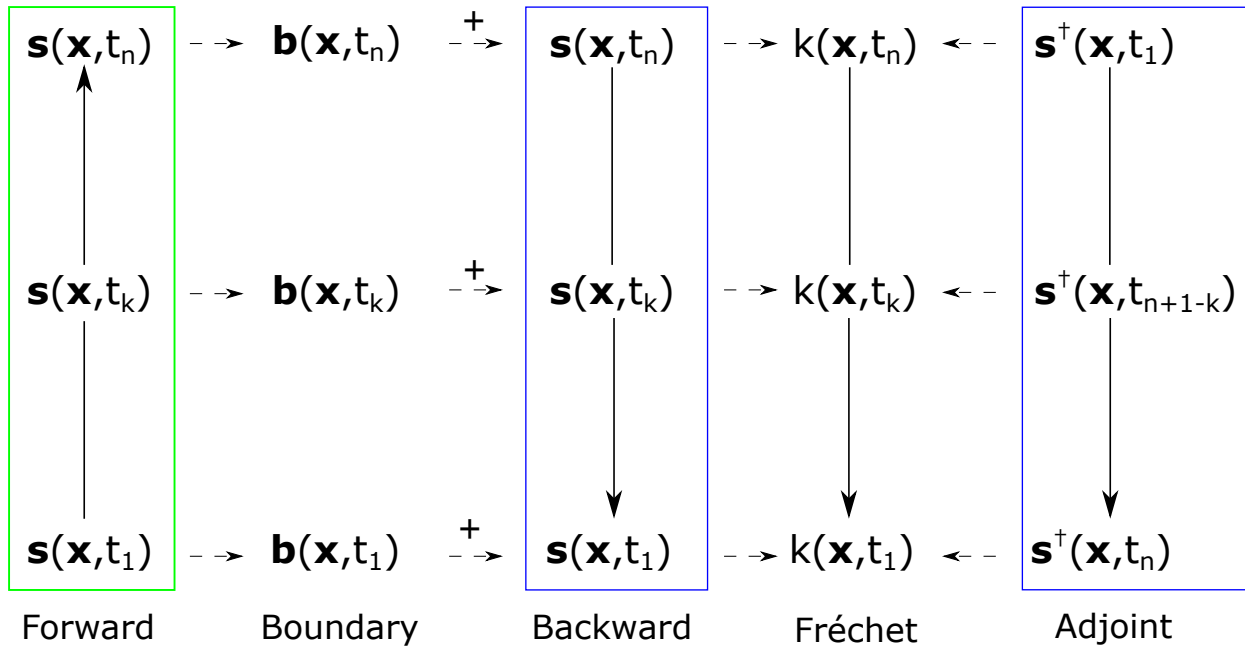


**Figure S1.** Forward simulation (green rectangle) and the simultaneous backward and adjoint simulation (blue rectangles) for computing the Fréchet kernels. The forward simulation is started from the first time step  $t_1$  and ended at the last time step  $t_n$ . The absorbing boundary field  $\mathbf{b}(\mathbf{x}, t_k)$  of each time step  $t_k$  and the last state field  $\mathbf{s}(\mathbf{x}, t_n)$  are stored in the forward simulation. The backward simulation takes the last state field as a start point and reconstructed the forward field backward in time. In each time step, the absorbing boundary field  $\mathbf{b}(\mathbf{x}, t_k)$  is re-injected into the backward simulation to reconstruct the forward fields (called backward fields here). The adjoint simulation is started from the time-reversed adjoint source from the receivers. The Fréchet kernels at each time step or at a sub-sampled time step are constructed on the fly based upon the backward and adjoint fields. If each time step is used, the kernels are summed at each time step until the final step as  $K_m = \sum_{k=1}^n \mathbf{K}(\mathbf{x}, t_k) \delta t$ , where  $\delta t$  is time interval in the simulation.

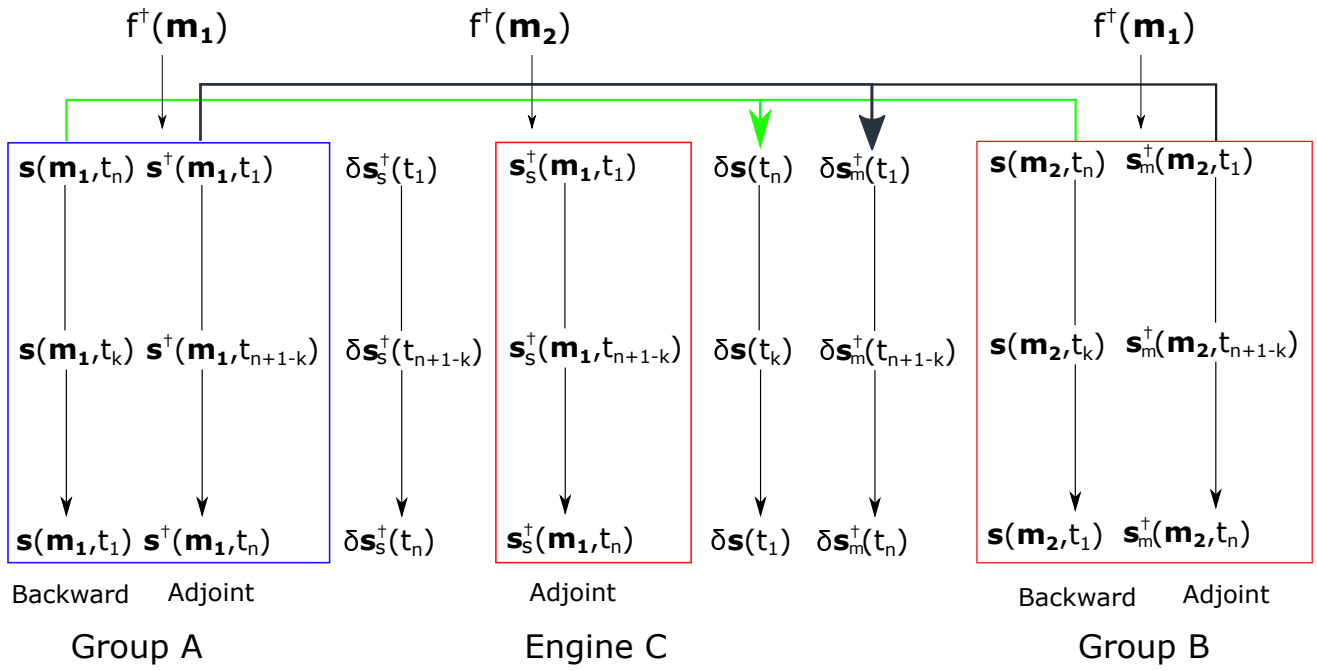


**Figure S2.** Simultaneous backward and adjoint simulation in the Multi-SEM, where five SEM solvers are coupled and used (see the five arrows within the three rectangles). Group A: two SEM solvers are coupled and used under the same mesh database, where one solver is used for the backward simulation and the other solver is used for the adjoint simulation. This is similar to the adjoint simulation in the computation of Fréchet kernels. Group A is designed to compute the backward and adjoint fields for model  $\mathbf{m}_1$ . On the right side, Group B adopts two SEM solvers to compute the backward and adjoint fields for the perturbed model  $\mathbf{m}_2$ . Engine C is one solver engine designed to compute the adjoint field due to the perturbation of the adjoint source  $f^+(\mathbf{m}_2)$ . The simulation in Engine C is the same as the adjoint simulation of Group A except the source term. Since all the fields are computed on the fly for each designed time step (each time step or a skipping time step), the perturbed fields to be used in the calculation of Hessian kernels can be determined, e.g., by the first-order finite-difference approximation.

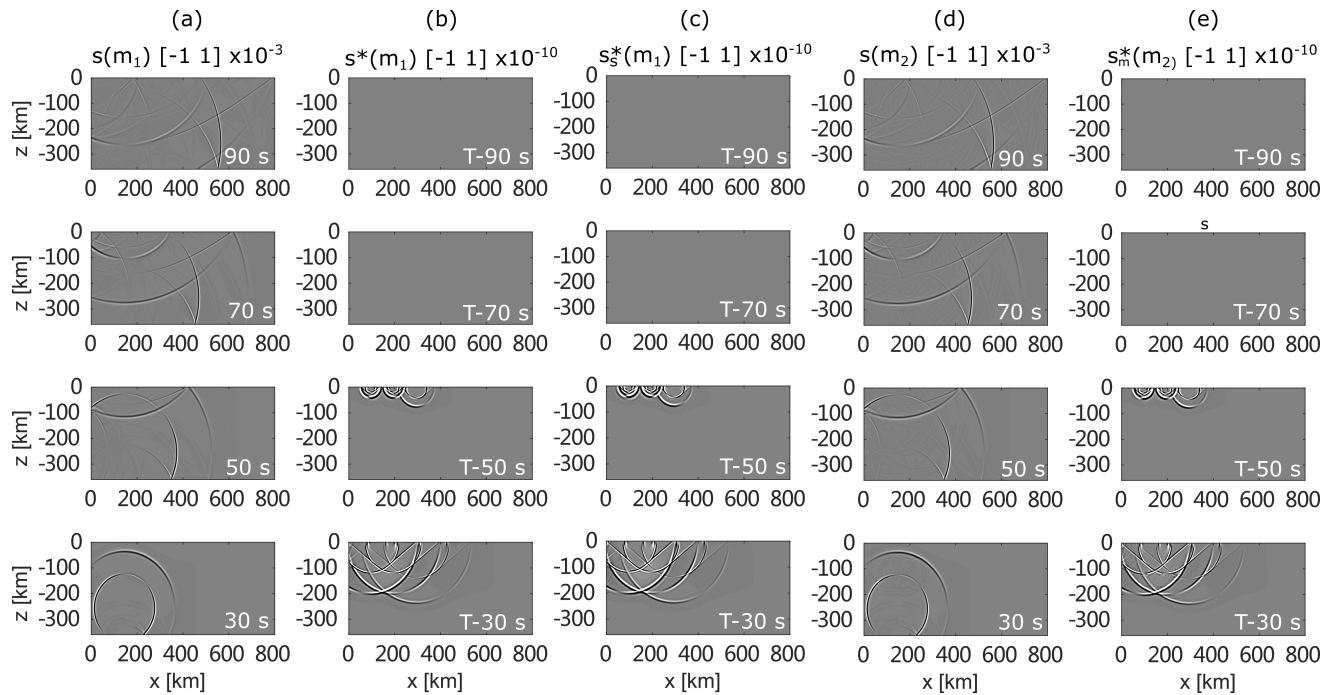


**Figure S3.** Four selected time steps of the five wavefields computed by Multi-SEM. (a) The forward fields recorded at times 30 s, 50 s, 70 s, and 90 s for model  $\mathbf{m}_1$ . (b) The adjoint fields for the same model but recorded at reversed times of T-90 s, T-70 s, T-50 s, and T-30 s, where  $T = 100$  s in this example. (c) The adjoint fields generated by the adjoint source computed from the measurements for  $\mathbf{m}_2$ . (d) and (e) show the similar simulation as (a) and (b) but for the perturbed model  $\mathbf{m}_2$ , instead of  $\mathbf{m}_1$ . (b) and (e) looks similarly due to the use of the same adjoint source but they are different after the adjoint fields traveling through the scatter.

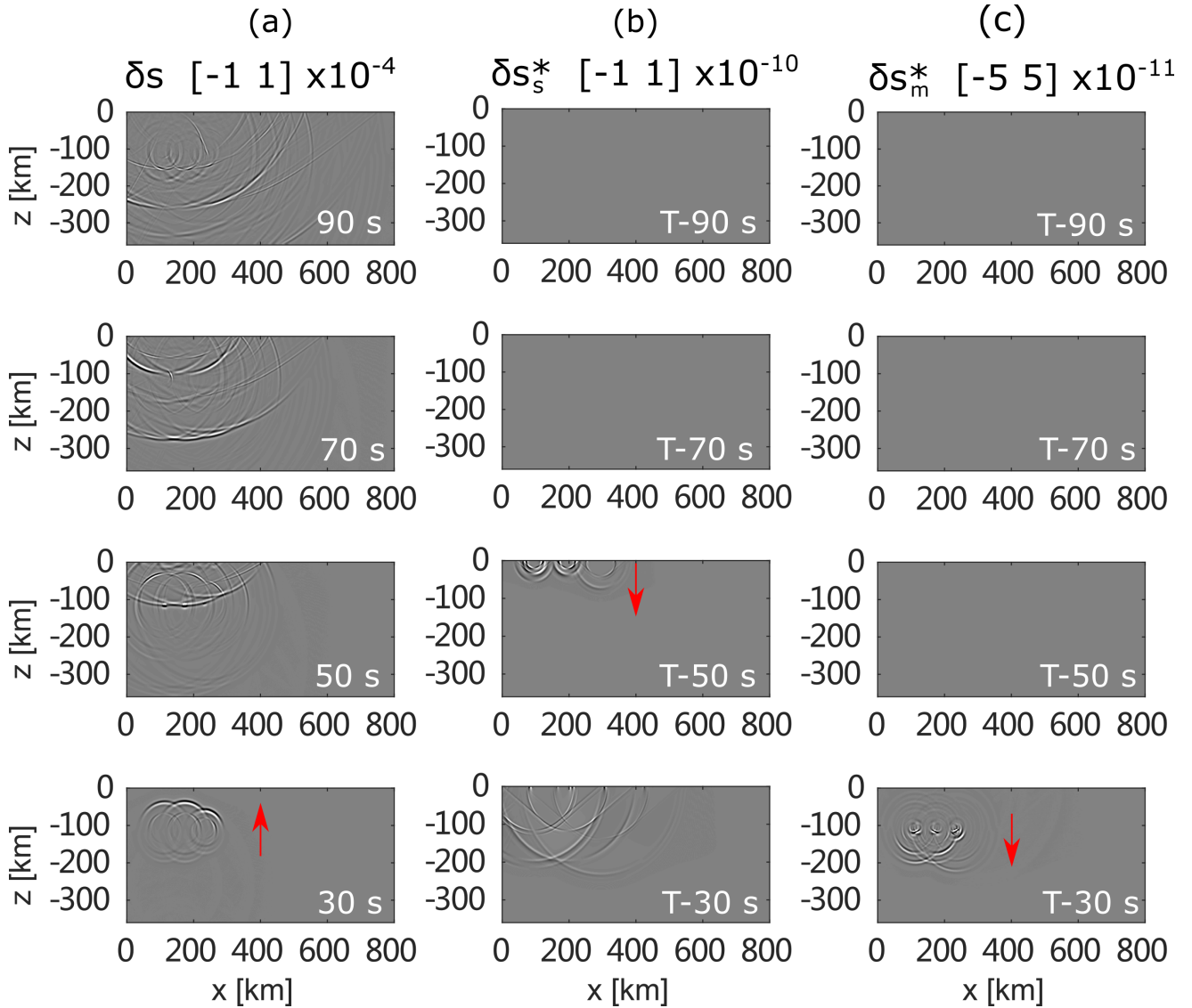


**Figure S4.** A few time steps of selected perturbed fields computed on the fly using the first-order finite-difference approximation. (a) Perturbed forward fields. (b) Perturbed adjoint fields due to the perturbation of the adjoint source. (c) Perturbed adjoint fields due to the perturbation of the model. The perturbed fields, e.g., generated around the red arrows are due to the perturbations either from the model or from the adjoint source.

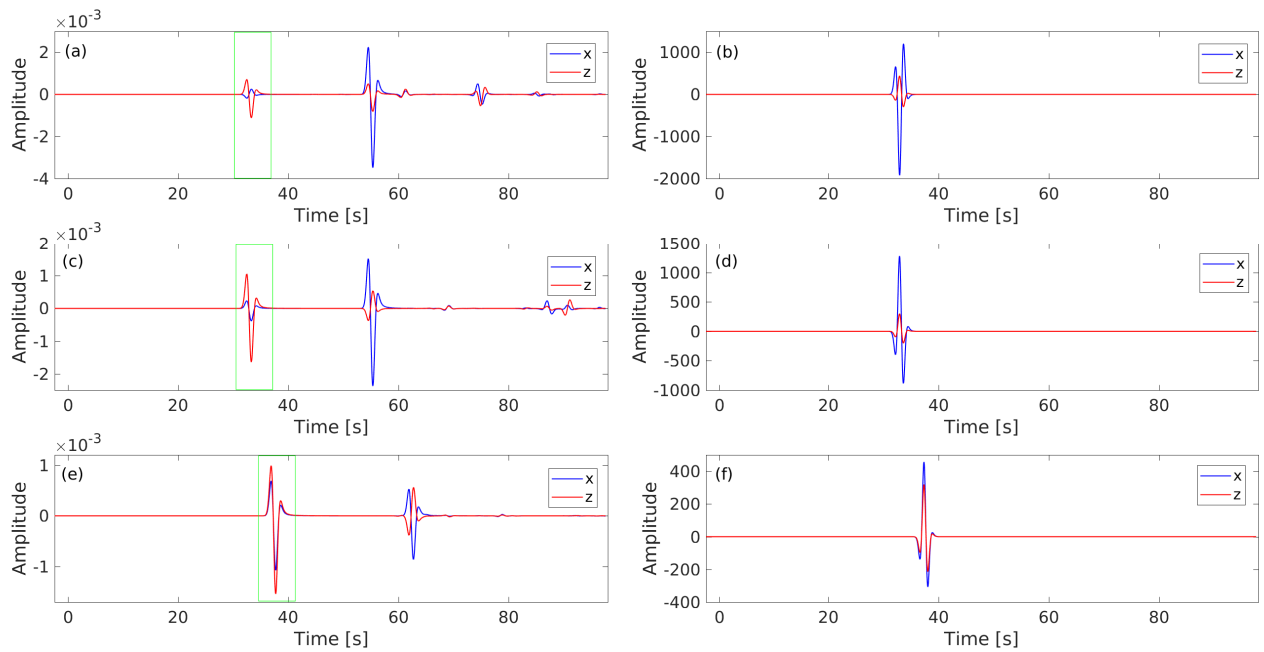


**Figure S5.** Two-component seismograms registered at the three stations (a,c,e) and their associated adjoint source (b,d,f) computed for the first P wave peak (green rectangles). This example uses the homogeneous model and the traveltime adjoint source.

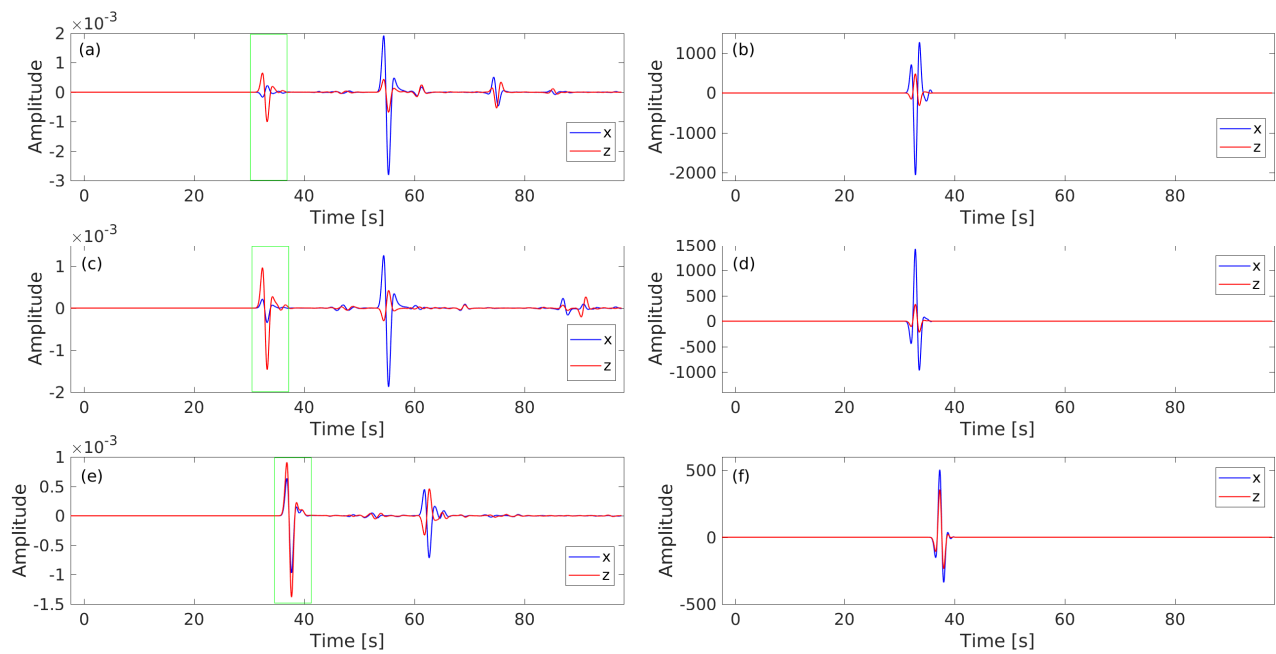


**Figure S6.** Two-component seismograms registered at the three stations (a,c,e) and their associated adjoint source (b,d,f) computed for the first P wave peak (green rectangles). This example uses the perturbed model with three scatters and the traveltime adjoint source.

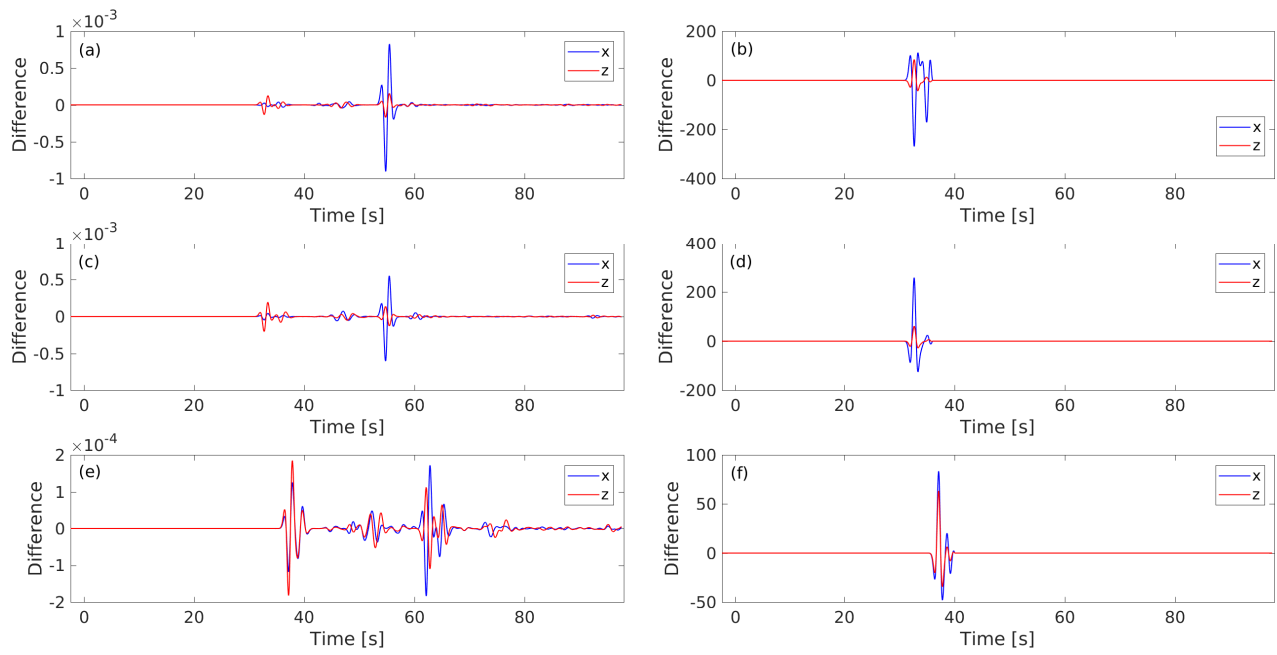


**Figure S7.** The differences between Figure S6 and Figure S5 (i.e., Figure S6 - Figure S5), which is designed to see the differences in terms of seismograms and adjoint sources due to the perturbation of the model.

Forward output	Backward and adjoint output
Database*****.bin	
absorb_elastic_bottom*****.bin absorb_elastic_left*****.bin absorb_elastic_right*****.bin absorb_elastic_bottom_m2_*****.bin absorb_elastic_left_m2_*****.bin absorb_elastic_right_m2*****.bin	proc*****_rho_kappa_mu_kernel.dat proc*****_rho_kappa_mu_kernel_Ha.dat proc*****_rho_kappa_mu_kernel_Hbm.dat proc*****_rho_kappa_mu_kernel_Hbs.dat proc*****_rho_kappa_mu_kernel_Hc.dat proc*****_rho_kappa_mu_kernel_Habc.dat
AA.S****.BXX.semd AA.S****.BXZ.semd AA.S****.BXX.semd_m2 AA.S****.BXZ.semd_m2	proc*****_rhop_alpha_beta_kernel.dat proc*****_rhop_alpha_beta_kernel_Ha.dat proc*****_rhop_alpha_beta_kernel_Hbm.dat proc*****_rhop_alpha_beta_kernel_Hbs.dat proc*****_rhop_alpha_beta_kernel_Hc.dat proc*****_rhop_alpha_beta_kernel_Habc.dat
lastframe_elastic*****.bin lastframe_elastic_m2_*****.bin	

**Figure S8.** Some important files output from the forward simulation and the simultaneous backward and adjoint simulation in the Multi-SEM package. The left column shows the files output from the forward simulation. The first row shows the meshing database which includes the internal model to be replaced by the two external models before the main time loop in the simultaneous backward and adjoint simulation. The second row shows the absorbing boundary fields, where the shadow part indicates files output for the perturbed model  $\mathbf{m}_2$ . The third and fourth rows show the seismograms registered at the receivers and the last state of the forward field. These files output in the forward simulation will be used in the simultaneous backward and adjoint simulation. The right column shows the key files output in the simultaneous backward and adjoint simulation, including the Fréchet kernels, the approximate Hessian kernels ('Hbs'), and the full Hessian kernels ('Habc'), etc. In the right column, the top part shows for the  $(\rho, \kappa, \mu)$  parameter set and the bottom part shows for the  $(\rho, \alpha, \beta)$  parameter set.

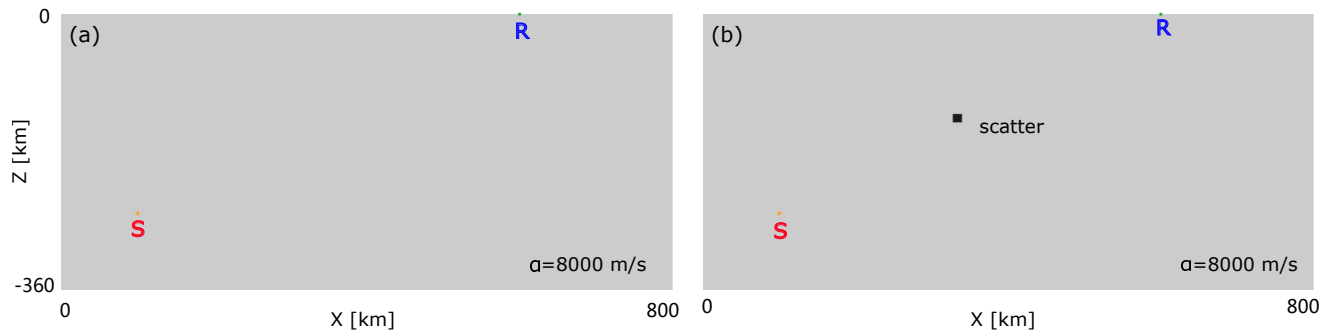


**Figure S9.** Homogeneous model (a) and the perturbed model with one scatter (b) for compressional wave speed  $\alpha$ , where S indicate the source location and R denotes the receiver location. Relative model perturbation for the scatter is set to +10% for the  $\alpha$  and  $\beta$  over the homogeneous model.

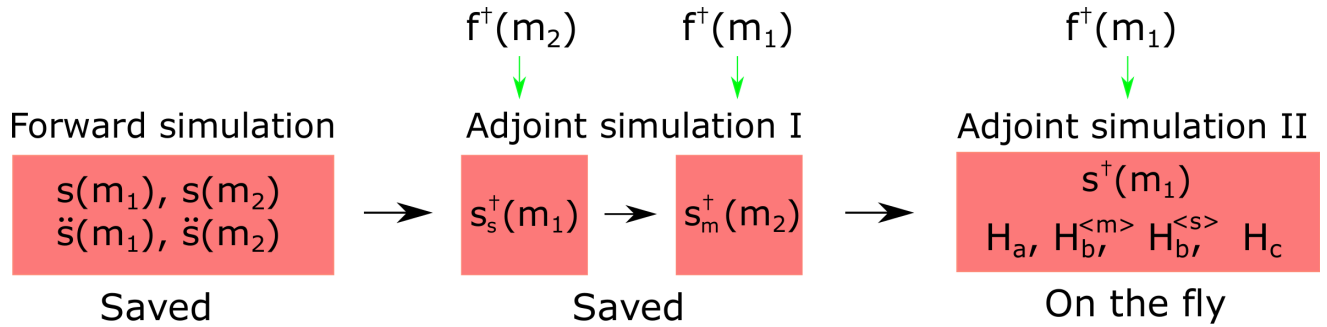


**Figure S10.** A workflow illuminating the computation of the Hessian kernels by the required forward and adjoint fields. The first step (Forward simulation) is to compute and save the forward fields, the second step (Adjoint simulation I) is to compute and save the two adjoint fields. The last step (Adjoint simulation II) is to compute one adjoint field  $\mathbf{s}^+(\mathbf{m}_1)$  on the fly, and read one time step of the saved four or six fields into the temporary memory for the computation of Hessian kernels. The case for the four fields is to compute the Hessian kernels without density perturbation consideration. The  $\mathbf{f}^+(\mathbf{m}_1)$  and  $\mathbf{f}^+(\mathbf{m}_2)$  denote the two adjoint sources computed from the measurements of the two models, which are used to generate the adjoint fields.

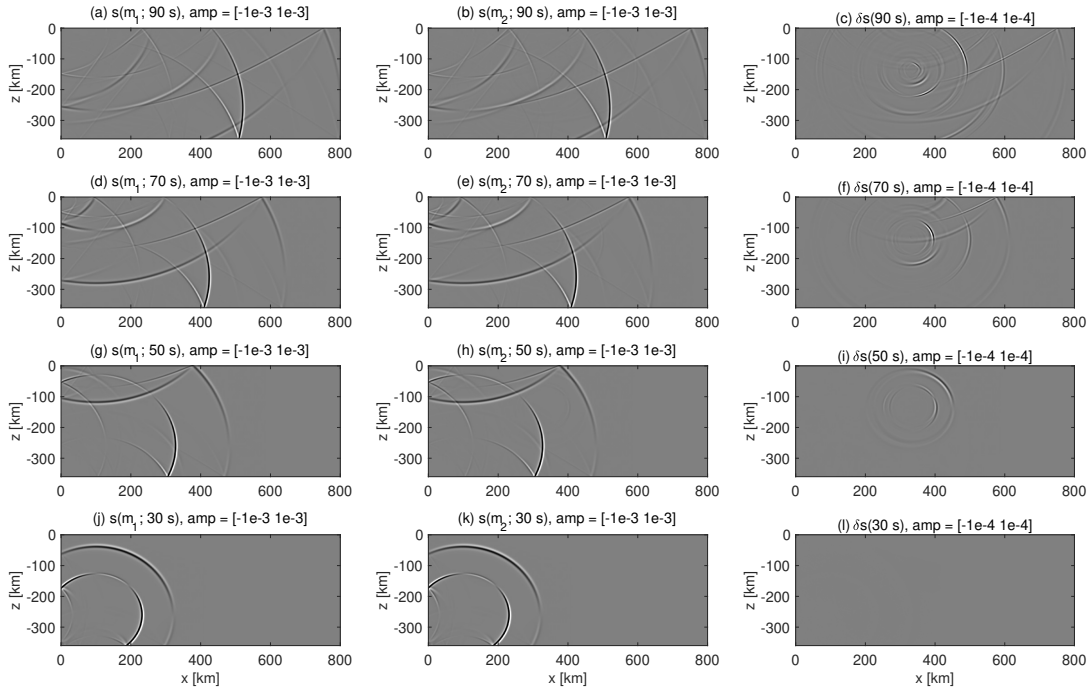


**Figure S11.** Four time steps of the two forward fields  $\mathbf{s}(\mathbf{m}_1)$  and  $\mathbf{s}(\mathbf{m}_2)$  and their perturbations  $\delta\mathbf{s}$  due to the scatter. The first column shows the forward fields  $\mathbf{s}(\mathbf{m}_1)$  for  $\mathbf{m}_1$ . The second column shows the forward fields  $\mathbf{s}(\mathbf{m}_2)$  for  $\mathbf{m}_2$ . For simplicity, we omit the time dependencies. The perturbed wavefields are computed by using the wavefield subtraction, i.e.,  $\mathbf{s}(\mathbf{m}_2) - \mathbf{s}(\mathbf{m}_1)$ .

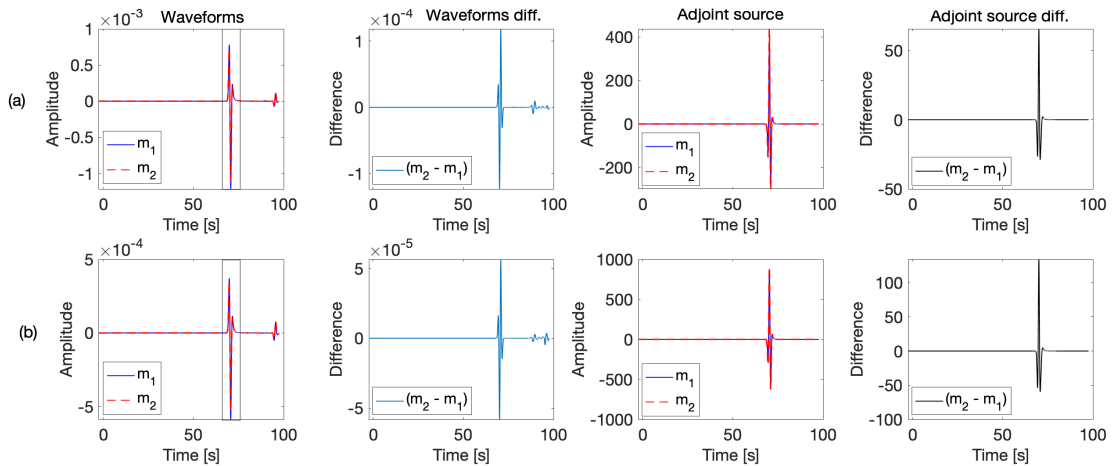


**Figure S12.** Waveforms and traveltime adjoint sources computed for model  $\mathbf{m}_1$  and  $\mathbf{m}_2$ . Narrow phase-shifted (Ricker) waveforms are observed due to an illumination for the entire time period. The first row (a) shows the  $x$  components for the two models. For simplicity, only the P wave (within the time window) is used for computing the adjoint source (see the rectangle window left up). The second row shows the  $z$  components for the two models. For the two modes, we also compute the waveform difference (second column) and the adjoint source difference (fourth column) to see the wave difference in magnitude due to the perturbation of the model.

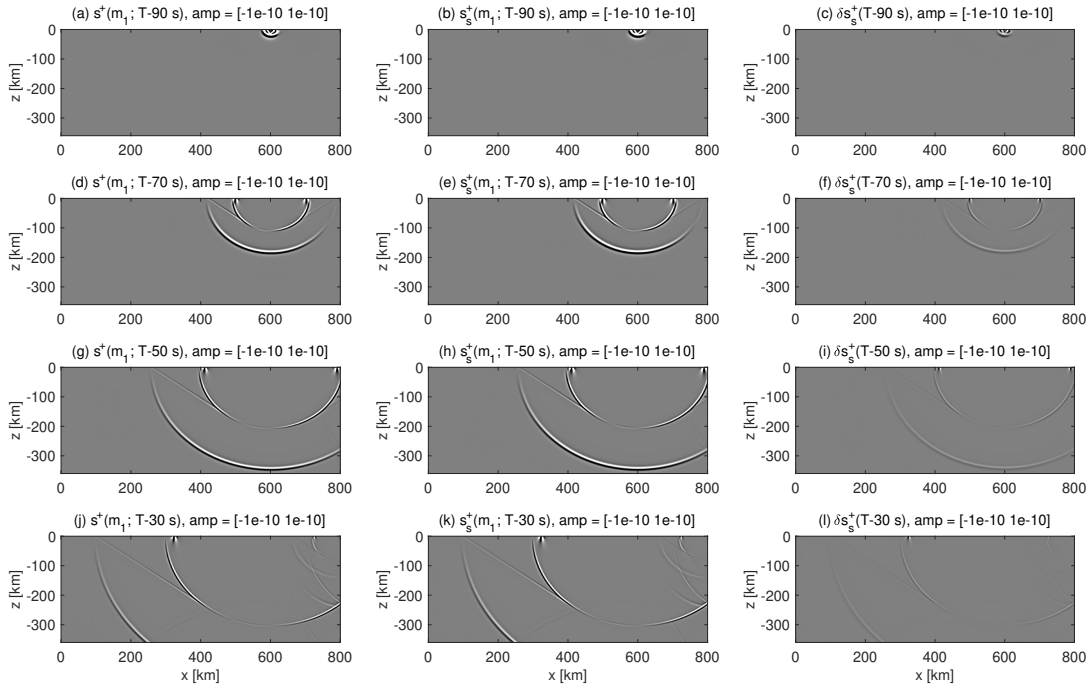


**Figure S13.** Four time steps of the adjoint fields  $\mathbf{s}^{\dagger}(\mathbf{m}_1)$  and  $\mathbf{s}_s^{\dagger}(\mathbf{m}_1)$  and their perturbations  $\delta \mathbf{s}_s^{\dagger}$ . The first column shows the adjoint field  $\mathbf{s}^{\dagger}(\mathbf{m}_1)$  for model  $\mathbf{m}_1$ . The second column shows the adjoint field  $\mathbf{s}_s^{\dagger}(\mathbf{m}_1)$  for the same model  $\mathbf{m}_1$ . The third column shows their associated perturbed fields  $\delta \mathbf{s}_s^{\dagger}$  computed by the wavefield subtraction.

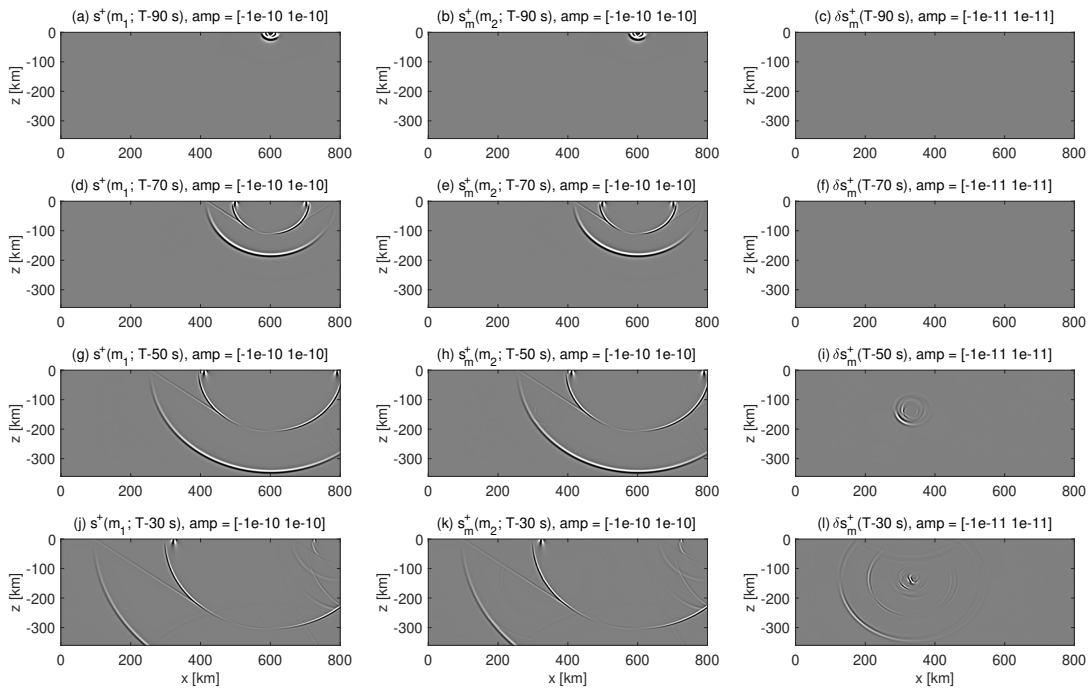


**Figure S14.** Four time steps of the adjoint fields  $s^{\dagger}(\mathbf{m}_1)$  and  $s_m^{\dagger}(\mathbf{m}_2)$  and their perturbations  $\delta s_m^{\dagger}$ . The first column shows the adjoint field  $s^{\dagger}(\mathbf{m}_1)$  for model  $\mathbf{m}_1$ . The second column shows the adjoint field  $s_m^{\dagger}(\mathbf{m}_2)$  for model  $\mathbf{m}_2$ . The third column shows their perturbed fields  $\delta s_m^{\dagger}$  computed by the wavefield subtraction.

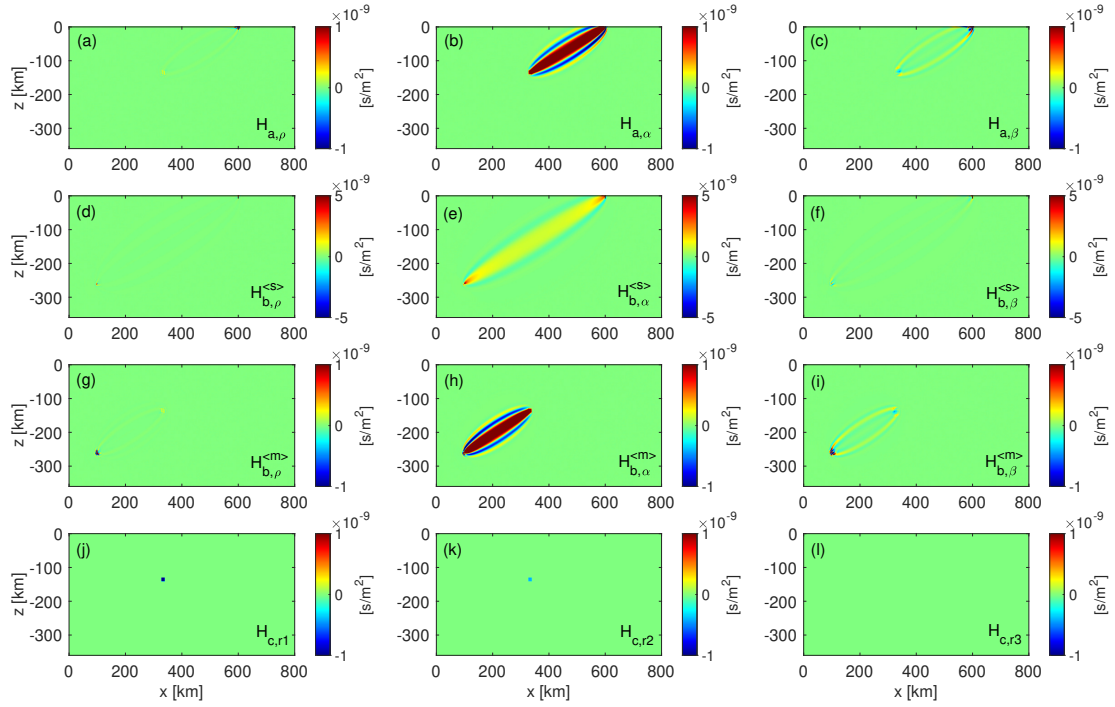


**Figure S15.** Four components of the Hessian kernels with respect to the model given in  $\rho$ ,  $\alpha$ , and  $\beta$ . The top first row shows the  $H_a$  component with respect to the three models parameters. Only the  $H_{a,\alpha}$  is well observed since only the P phase is used for the adjoint source calculation. The second rows shows the  $H_b^{(s)}$  component, which is approximate Hessian kernels due to the perturbation of the adjoint source to the adjoint field. The third row shows the  $H_b^{(m)}$  component which is due to the perturbation of the model for the adjoint field. The bottom row shows the  $H_c$  component. Only the kernels for  $H_{c,r1}$  and  $H_{c,r2}$  are observed since the  $K_\beta$  equals to zero. The  $ri$  (where  $i = 1, 2, 3$ ) indicates the three rows in the  $H_c$  expression. The full Hessian kernels are obtained by summing the four components together.

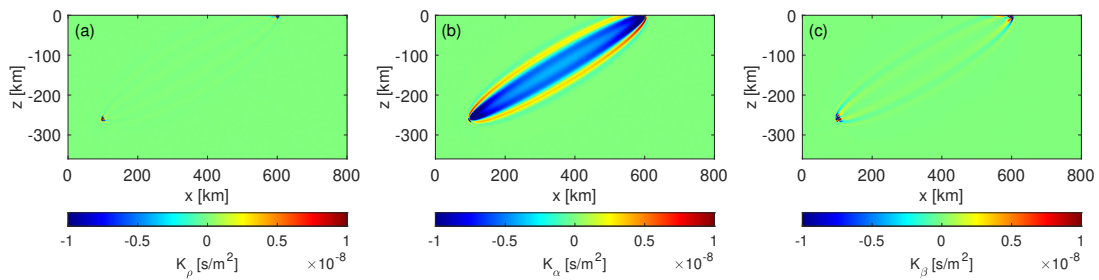


**Figure S16.** Three components of the Fréchet kernels for the homogeneous model. Only the  $K_\alpha$  is well observed since only the P phase is used in the adjoint source calculation. Some artefacts observed near the source and receiver in the  $K_\rho$  and  $K_\beta$  components.

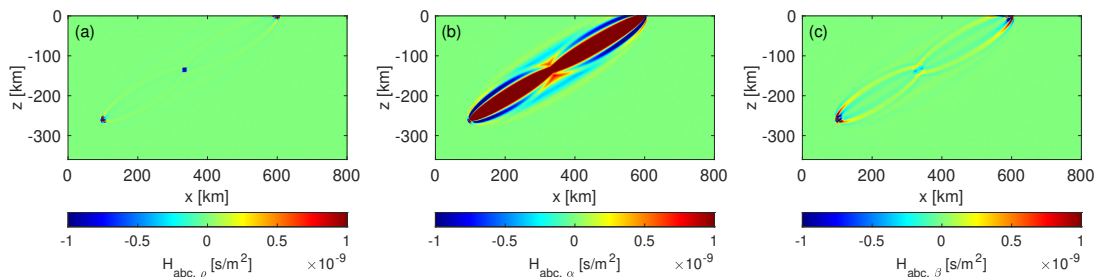


**Figure S17.** The Hessian kernels with respect to the model parameters  $\rho$ ,  $\alpha$ , and  $\beta$ . The figure is a summation of each row of Figure S15. Significant differences are observed between the full Hessian kernels and the approximate Hessian kernels as well as the Fréchet kernels (see Fig S15 to Fig S17). The different color is due to the minimum and maximum color values set for the kernels.